Title

Velocity-based optoretinography for clinical applications.

Journal

Optica, 9(10)

ISSN

2334-2536

Authors

Vienola, Kari

Valente, Denise

Zawadzki, Robert

et al.

Publication Date

2022-10-20

DOI

10.1364/optica.460835

Peer reviewed

Published in final edited form as:

Optica. 2022 October 20; 9(10): 1100–1108. doi:10.1364/optica.460835.

Velocity-based optoretinography for clinical applications

Kari V. Vienola[1], **Denise Valente**[1], **Robert J. Zawadzki**[1,2], **Ravi S. Jonnal**[1,*]

[1]Vision Science and Advanced Retinal Imaging Laboratory, Department of Ophthalmology and Vision Science, University of California, Davis, Sacramento, California 95817, USA

[2]EyePod: Small Animal Ocular Imaging Laboratory, Department of Cell Biology and Human Anatomy, University of California, Davis, Davis, California 95816, USA

Abstract

Optoretinography (ORG) is an emerging tool for testing neural function in the retina. Unlike existing methods, it is noninvasive and objective, and provides information about retinal structure and function at once. As such, it has great potential to transform ophthalmic care and clinical trials of novel therapeutics designed to restore or preserve visual function. Recent efforts have demonstrated the feasibility of ORG using state-of-the-art optical coherence tomography systems. These methods measure the stimulus-evoked movement of subcellular features in the retina, using the phase of reflected light to monitor their positions. Here we present an alternative approach that monitors the velocity of these features instead. This conceptual shift has significant implications for the nascent field of ORG. By avoiding the need to track specific cells over time, it obviates costly and laborious aspects of position-based approaches, such as adaptive optics, digital aberration correction, real-time tracking, and three-dimensional segmentation and registration. We used this velocity-based approach to measure the photoreceptor ORG responses in three healthy subjects. The resulting responses were reproducible and exhibited dependence on dose and retinal eccentricity. The possibility of reconstructing the position signal through numerical integration of velocity was explored.

1. INTRODUCTION

Visual information is gathered in the retina by photoreceptors as they absorb photons and convert their energy into membrane potentials in a process known as phototransduction. The resulting signal propagates through several classes of retinal interneurons before being transmitted to the brain via the optic nerve. An overview of the eye's anatomy and the location of the retina is shown in Fig. 1(a). Assessment of the visual process and its cellular mechanisms is indispensable for disease assessment in the clinic and in studies of the mechanisms of disease and efficacy of therapeutic interventions. To that end, a variety of psychophysical and electrophysiological tests have been used. Some of these, such as eye charts and perimetry, are subjective, in the sense that they require feedback from the patient regarding the visibility of stimuli. Subjective tests can be time consuming and suffer from spurious sources of variance such as attention and learning effects. Others, such as the

*Corresponding author: rjonnal@gmail.com.

Disclosures. The authors declare no conflicts of interest.

electroretinogram (ERG) [1], permit objective measurement of stimulus-evoked electrical activity, but are moderately invasive, requiring placement of electrodes on the cornea and face.

In addition to assessing visual function, clinicians need to observe how retinal structure is affected by disease. Historically, this was done with slit lamp exams and fundus photography, but over the past two decades, optical coherence tomography (OCT) has become a standard of ophthalmic care. With OCT, the laminar structure of the retina can be visualized noninvasively in three dimensions [Fig. 1(b)] [2]. Even with much progress in the development of tools for both functional and structural assessment, a need exists for an objective, noninvasive assay of retinal function, ideally capable of simultaneously observing the structure of the retina.

As an interferometric imaging modality, OCT records the amplitude and phase of light reflected by the retina. The familiar OCT image is created using only the signal amplitude, and the phase is normally disregarded. However, the phase of the signal contains information about the position of scattering objects in the scene, and is thus sensitive to tissue movement, even if it is much smaller than the optical resolution of the imaging system [3]. Sensitivity to the movement of a structure depends on its reflectivity: for the brightest features in the ophthalmic OCT image, movements as small as a few nanometers may be measured. This level of sensitivity requires computational methods to correct for the confounding phase shifts caused by eye motion [4,5].

Because neurons are known to swell and shrink during signaling, phase-sensitive OCT offers the ability to detect whether these cells are responding to stimuli. Early efforts to observe these stimulus-evoked responses in human cone photoreceptors used adaptive optics (AO), which permitted resolution and tracking of single cells, in conjunction with common path interferometry [6]. Since then, interest in this area has grown, and these responses have been successfully measured in cones using detection schemes such as full-field swept-source OCT with digital aberration correction (DAC) [7], flying-spot AO-OCT [8,9], and line-scanning OCT and AO-OCT [10]. Responses have also been measured in rods, using a multimodal AO-OCT system [11]. These cutting-edge systems all provide measurements of neural responses at the level of single cells, where characteristics of the response may be studied in detail and where disease-related dysfunction manifests earliest. The most commonly reported method has been to localize the two boundaries of the photoreceptor outer segment (OS)—the inner-OS junction (IS/OS) and the cone or rod OS tip (COST or ROST)—and monitor the difference between the phase of light returning from the two structures [5] [see Figs. 1(c) and 1(d)]. This novel way to observe photoreceptor responses in the retina has been termed *optoretinography* (ORG) [12,13], and it has been successfully used to classify cones by spectral properties [9] and to detect cone dysfunction in retinitis pigmentosa patients [14].

To our knowledge, the ORG is the only noninvasive, objective test of neural function in the retina that can simultaneously reveal its structure, making it ideal for ophthalmic care and clinical research. However, the sophisticated imaging and processing methods used to prove the ORG concept pose challenges for clinical translation. The systems utilizing AO require

expensive components and incur additional costs in personnel due to their optical complexity and need for multiple expert operators. In addition, the data rates of these instruments can be as high as tens of gigabytes per second, which at present, in conjunction with the required data processing, precludes rapid test results. Together, these constraints limit the number of healthy and disease-affected eyes that can be tested, and thus the translational utility of the test.

Here, we present a novel ORG approach using a custom OCT system very similar to those currently employed in the clinic. Unlike the research systems described above, it lacks the ability to resolve and track single cells. Instead, the signal processing pipeline was designed around the assumption that the exact cells being imaged at any given time may move out of the field of view at other times. When this happens, the phase difference between the IS/OS and COST reflections is affected not only by light-induced deformation of the OS (i.e., the meaningful ORG signal intended for measurement), but also by random variation in the OS length among neighboring cells. The latter source of noise is unrelated to the cells' response to light, and may be orders of magnitude larger than the light-induced deformation. In the approach proposed here, phase changes in the IS/OS and COST layers were measured within a time window short enough to neglect retinal movement (<10 ms), and converted into instantaneous, depth-dependent tissue velocities. The stimulus color was selected to stimulate the overwhelming majority of cones (those of L and M spectral classes) identically, and the method depends on their correlated deformation velocities. That is, on time scales larger than 10 ms, when the observed OS lengths may vary considerably due to eye movements, the deformation velocities remain meaningfully related and form a concordant time series of photoreceptor response. This series of velocities is related, by integration, to the underlying average contraction and expansion rates of the cone OSs. Reconstruction of the tissue position may not be necessary anyway, since previous reports suggest that the derivative of the position signal (i.e., velocity) is a useful way to quantify it [10,11].

2. METHODS

A. Optical Coherence Tomography System

The OCT system is illustrated in Fig. 2(a). It used a 1060 nm swept-source (SSOCT; Axsun; Billerica, MA, USA), with a 100 kHz A-scan rate and 100 nm bandwidth. A fiber Bragg grating (FBG) at the source output generated a notch in the acquired spectra, used for spectral alignment of scans. Ten percent of the light from the source was directed to the sample arm, where it was collimated (AC080–10-B; Thorlabs; Newton, NJ, USA) before passing through the galvanometric scanners (6210 H & 8310 K; Cambridge Technology; Bedford, MA, USA) and a demagnifying telescope (f_{L1} = 100 nm, f_{L2} = 75 mm), creating a 1.2 mm beam on the cornea (pupil plane). The last lens (L2) can be translated to correct defocus. Ninety percent of the source light was directed to the reference arm where it propagated through a polarization controller and dispersion-compensating fiber patch cord. The backscattered light from the eye was combined with the reference arm using a 50/50 fiber coupler. The reference arm power was adjusted using an aperture [A_1 in Fig. 2(a)],

and a retroreflector was translated in one dimension to adjust the reference arm length. The optical power for the OCT in the sample arm at the pupil plane was measured to be 1.8 mW.

To deliver a temporally controlled stimulus flash to the retina, a fiber-coupled 554 nm light emitting diode (MINTF4; Thorlabs; Newton, NJ, USA) was used. Light exiting the fiber was collimated and filtered using a 23 nm bandpass filter centered at 555 nm (FF01–554/23; Semrock; Lake Forest, IL, USA). The stimulus light was combined with the OCT beam path using a dichroic beam splitter (T715lp; Chroma; Bellows Falls, VT, USA). The stimulus light passes through a non-magnifying telescope ($f_{L3,L2}$ = 75 mm) before entering the eye. The diameter of the stimulus was approximately 360 μm on the retina, smaller than the imaged region. The mismatch arose because the light source was powerful enough to bleach only 15% of photopigment in a circular region with a diameter of 750 μm. The 555 nm stimulus wavelength was selected because it isomerizes L- and M-photopigments equally, which make up the overwhelming majority of cones [15].

The voltage signal from the balanced detector (PDB481C-AC; Thorlabs; Newton, NJ, USA) was filtered with a 150 MHz low-pass filter (SLP-150+; Mini-Circuits; Brooklyn, NY, USA) and attenuated by 15 dB (VAT-15 +; Mini-Circuits; Brooklyn, NY, USA) before being sampled at 12 bits with a ± 400 mV range using a digitizer (ATS9350; AlazarTech; Pointe-Claire, QC, Canada). The swept-source provided timing signals from its *k*-clock and sweep trigger to the digitizer. The analog waveforms to control the galvanometric scanners were generated using a multifunction data acquisition card (NI6251; National Instruments; Austin, TX, USA), and the OCT data acquisition was synchronized with the waveform generation.

The OCT software was developed in C ++ and CUDA and has been previously published [16]. When the OCT acquisition started, a 5 V trigger pulse was sent to a function generator (DG4202; RIGOL; Suzhou, JS, China), which then sent the preconfigured stimulus signal to the LED controller (DC4100; Thorlabs; Newton, NJ, USA). By setting the delay, width, and amplitude of this signal, the stimulus flash could be modified to bleach the desired percentage of photopigment.

B. Calculating Photopigment Bleaching

Photopigment bleaching can be calculated using the equation [17]

$$p(t) = A_0 e^{-\frac{T}{Q_e}t}, \tag{1}$$

where A_0 is the initial amount of the photopigment, $p(t)$ is the fraction of the remaining photopigment, T is the conventional illuminance of the stimulus flash in Trolands (Td), t is the duration of the stimulus (in seconds), and Q_e is the conventional luminous exposure (in Td · sec) needed to deplete the photopigment to $1/e$. We used the value of 2.4×10^6 Td · sec for Q_e, following Rushton and Henry [17]. The conventional retinal illuminance T can be calculated from the luminous power using the following equation [18]:

$$T = P_{\mathrm{v}}\Omega^{-1} \times 10^{6}, \tag{2}$$

where P_{v} is the photopic luminous power in lumens, and Ω is the solid angle measured from the nodal point of the eye. To convert our radiometric measurement into photometric units, we use

$$P_{\mathrm{v}} = K_{\mathrm{m}} \int_{\lambda_1}^{\lambda_2} P_{\mathrm{e}}(\lambda) V(\lambda) \mathrm{d}\lambda, \tag{3}$$

where K_{m} is a conversion constant equal to 683 lm/W, P_{e} is the radiant power, and $V(\lambda)$ is the photopic luminous efficiency function. For simplicity, we assumed our light to be monochromatic with λ_{c} = 555 nm, resulting in $V(\lambda)$ of one. Finally, by combining Eqs. (2) and (3), we get

$$T = 683 \times P_{\mathrm{e}}\Omega^{-1} \times 10^{6} = 683 \times P_{\mathrm{e}}\left(\frac{A}{r^2}\right)^{-1} \times 10^{6}, \tag{4}$$

where the unit of P_{e} is the radiant power in watts, A is the illuminated area, and r is the distance from the eye's nodal point to the retina (which we assumed to be 17 mm). As the stimulus size on the retina has a diameter of 360 μm, we have all the information needed to convert the optical power measured from the pupil plane into Trolands, and then use it in Eq. (1). The resulting bleaching levels and corresponding optical powers are listed in Table 1.

C. Imaging Protocol

All imaging procedures were in accordance with the Declaration of Helsinki and were approved by the UC Davis Institutional Review Board. Written informed consent was obtained from all participants following an explanation of experimental procedures and risks, both verbally and in writing. To ensure safe imaging, the laser safety limits were calculated using the latest standard [19].

The use of mydriatic drops was not necessary. A custom bite bar was fabricated for each subject to position and stabilize their head. For ORG measurements, subjects were dark adapted for 5 min and then asked to look into the system and fixate on the fixation target [Fig. 2(a)]. The OCT system was configured to scan in one dimension only, acquiring a series of B-scans in a single location. B-scans consisting of 250 A-scans (scan width approx. 750 μm) were collected at a rate of 400 Hz. B-scans were collected before and after the stimulus flash, with the 40 scans before and after the flash used for subsequent analysis. The stimulus size was controlled by an aperture and set to 3.5 mm at the pupil-conjugate plane, intended to prevent clipping by the iris and allowing all the stimulus power to reach the retina.

Two experimental parameters were explored: distance from the foveal center and stimulus dose. For distance, a total of 20 retinal loci were imaged after each period of dark adaptation. The multiple loci lay in concentric, iso-eccentric rings, with measurements taken at 5 loci for each distance. For the dose dependency, the stimulus power was changed after each dark adaptation round.

All measurements were done on the temporal side of the retina at distances of 2°, 4°, 6°, and 8° away from the foveal center. A total of three different subjects were used in this study, all having healthy maculae. Images were acquired at each of the four distances from the fovea, in all three subjects. In one of the subjects, the stimulus dose was varied to achieve six different L/M-photopigment bleaching levels, between 0% and 66%, with ORG measurements collected at four retinal eccentricities for each bleaching level.

D. Signal Processing

The recorded signal was processed in two stages. First, the raw spectral data were converted into cross-sectional OCT images (B-scans), using well-established approaches in the OCT literature. In short, raw digitized spectra were aligned using the FBG notch to create phase-stable B-scans. After the alignment, DC-bias was estimated and removed. The spectra were then corrected for dispersion mismatch between the two interferometer arms using numerical dechirping, and complex-valued B-scans were generated by Fourier transforming the processed spectra. B-scans were flattened, such that the IS/OS and COST reflections lay at the same height for each A-scan in the image. Flattening was performed by linearly shearing the B-scan until the height of the IS/OS and COST peaks in the laterally averaged B-scan was maximized.

In the second stage, the ORG signal was extracted. Complex B-scans were converted into estimates of tissue velocity as follows [Fig. 2(b)]. A moving, 10 ms time window was used to select groups of five sequential B-scans at a time. A histogram-based bulk-motion correction algorithm [4] was utilized to compensate for the axial eye movement during the 10 ms interval, with motion corrected relative to the first B-scan in the series. After bulk-motion correction, the resulting complex data cube (V) may be described as

$$V(x,z,t) = A(x,z,t)e^{j\theta(x,z,t)}, \tag{5}$$

where x and z are the lateral and depth coordinates, respectively, and t is time within the window, i.e., 0 ms ≤ t 10 ≤ ms. The phase data cube (x, z, t) was unwrapped in the temporal dimension by adding or subtracting 2π to (x_p , z_q, t_r) to minimize | $\theta(x_p, z_q, t_r) - \theta(x_p, z_q, t_{r-1})$|, where t_r and t_{r-1} represent consecutive phase B-scans. This step was performed for each spatial coordinate pair (x_p, z_q) in the volume. After unwrapping, a rate of phase change was computed for each coordinate pair by performing a least-squares linear fit with respect to t, giving $\frac{\Delta\theta}{\Delta t}(x,z)$ in rad/s. From this, we calculated the instantaneous velocity for each spatial location:

$$\frac{\Delta z}{\Delta t}(x,z) = \frac{\Delta \theta}{\Delta t}(x,z) \cdot \frac{\lambda}{4\pi n}, \tag{6}$$

where λ = 1060 nm, and n = 1.38, the nominal refractive index of the eye. An amplitude B-scan, along with pseudocolor overlays of instantaneous pre- and post-stimulus velocities is shown in Fig. 2(c). The next step in quantifying the response was averaging both the B-scan amplitude and $\left(\frac{\Delta z}{\Delta t}(x,z)\right)$ in lateral dimension, giving instantaneous, depth-dependent measures of backscattering and velocity $\left(\frac{\Delta z}{\Delta t}(z)\right)$ respectively. By shifting the 10 ms window by one B-scan period (2.5 ms) at a time, a time series of depth profiles can be constructed, separately for reflectivity and velocity.

Both of these can be visualized in time–depth coordinates, as M-scans [see Fig. 2(d)]. Because the signal-to-noise ratios of the phase changes and velocities are highest when the OCT amplitude is high [3], velocity overlays are shown only for the portions of B-scans and M-scans above 10% of the maximum linear amplitude. The IS/OS and COST layers were always well above this threshold, so thresholding did not affect the computed velocities. For visualization of their velocities, however, it was helpful to exclude the pseudocolor velocities of the dimmest parts such as the nuclear layers and ganglion cell layer, where calculated velocities may have been dominated by phase noise instead of movement. From $\left(\frac{\Delta z}{\Delta t}(z,t)\right)$, the velocities of the IS/OS and COST layer movements were extracted, and the difference between them is the velocity of contraction/elongation of the OS in the region, which we term $v_{OS}(t)$ or simply $v(t)$ hereafter. For each experimental condition, multiple measurements of $v(t)$ were acquired. The time-varying mean and standard error of the mean (SEM) were calculated from these, and used to generate the plots in Fig. 4. Because $v(t)$ is derived from a block of B-scans, its value is the convolution of the instantaneous velocity with a block-sized rectangular function, which may lead to underestimates of the magnitude of the true velocity.

Preliminary examination of the data revealed a biphasic response [as shown in Fig. 3(d)]: an initial OS contraction ($v(t) < 0$) over the first 10 ms, followed by an elongation ($v(t) > 0$) that appeared to be somewhat stable between 20 and 40 ms. Motivated by these features, as well as our previous scanning ORG measurements [8,11], we devised several parameters to quantify the responses [illustrated in Fig. 3(d)]: the most negative velocity after stimulus (v_{min}), the greatest positive acceleration (a_{max}), and the time-averaged velocity between 20 and 40 ms after stimulus ($\bar{v}_{20,40}$). A virtue of these figures of merit is that they depend on data collected within 40 ms of the stimulus flash, thereby avoiding corruption by reflexes caused by the stimulus, such as blinks and saccades. For all measurements, the OS length was recorded as well.

To compare the present measurements of OS velocity to earlier ORG measurements, we reconstructed the OS length response by numerical integration of velocity. ORG responses described above were computed by laterally averaging the phase velocities of the IS/OS and

COST layers, which creates a trade-off between signal-to-noise ratio (SNR) and resolution. To quantify this trade-off, the ORG (signal/SNR) was quantified as a function of the extent of lateral averaging in the images.

3. RESULTS

Figure 3 illustrates an individual ORG measurement. The M-scan [Fig. 3(a)] shows the amplitude of backscattered light as a function of time and depth in gray scale with tissue velocity superimposed in pseudocolor. The OCT amplitude is plotted as a function of depth in Fig. 3(b), where the peaks originating from the IS/OS and COST are visible. The corresponding tissue velocities can be observed to change in Fig. 3(a), following onset of the stimulus flash (green line). The velocity changes seen in the inner retina and choroid coincide with vascular plexuses, and are thus presumably due to blood flow. The changes due to cone photoreceptor responses can be seen in the IS/OS and COST layers of the M-scan, especially when these velocities are plotted [Fig. 3(c)].

In the first 5 ms after bleaching, the IS/OS velocity becomes positive (corresponding to downward movement, in the M-scan) while the COST velocity becomes negative (corresponding to upward movement). The movement of these features toward one another is consistent with contraction of the OS. Over the subsequent 10 ms, the velocities of the two layers reverse, with the IS/OS moving upward and the COST moving downward, consistent with OS elongation. Subtraction of these velocities gives the rate of OS length change (v_{OS}) as seen in Fig. 3(d). The observed results are consistent with previous reports using AO, which showed that the OS contracts initially (<10 ms after stimulation), and elongates after that for >100 ms. Proposed figures of merit for quantifying ORG responses are illustrated in Fig. 3(d).

Figure 4 shows the velocity responses measured at different eccentricities in three different healthy subjects. Each blue line is an average of between five and 10 trials, with the gray area representing the SEM. A response was visible in all individual trials (as illustrated in Fig. 4), and can be seen in the average response across all subjects and eccentricities. Both the contraction and elongation magnitudes appear to scale with eccentricity, reducing toward the periphery in all three subjects. In many individual trials, velocity measurements became noisy around 70 ms after the stimulus flash, and this is evident in the larger SEM visible in that portion of several of the plots. We speculate that the noise is a consequence of reflexive eye movements that reduce the effectiveness of our bulk-motion algorithm. Since the following statistical analysis utilized B-scans collected within 40 ms of the stimulus onset, it was unaffected by this noise.

The eccentricity dependence of the response is visualized in Figs. 5(a) and 5(b). Here, parameters v_{min} and a_{max} are used to illustrate the trends. The most negative velocity (v_{min}), which corresponds to the largest rate of contraction, decreased in magnitude between 2°and 6°, with similar values at 6° and 8°. The maximum acceleration of OS elongation, (a_{max}), decreased in magnitude between 2°(1.5 to 2.1 μm/s^2) and 6°(1.1 to 1.5 μm/s^2). The velocities are also expressed as fractions of the OS length per unit time (right *y* axis, plotted in red), which flattens the dependence of both aspects of the response on eccentricity.

Dose dependence of the response is visualized in Figs. 5(c) and 5(d), using log scale for the *x* axis (bleaching). Figure 5(c) illustrates the dependence, at all eccentricities, of the contractile response on dose, with higher doses having the largest (most negative) velocities. Contractile velocities were very similar at doses of 0% and 4% while elongation velocities differed. When the elongation was quantified as the average velocity between 20 and 40 ms post-stimulus ($\bar{v}_{20,40}$), a similar trend was visible, with brighter stimuli resulting in faster elongation. In response to the brightest stimuli (66% bleaching), elongation velocities were in the range of 1.00 to 1.25 μm/s. Qualitatively, dose and response appear to have a log-linear relationship between 4% and 66% bleaching. In all panels of Fig. 5, data points are offset horizontally for readability.

Numerical integration of the OS velocity is shown in Fig. 6. The velocity of the rapid elongation stage, between approximately 10 and 100 ms, appears to be about 1 μm/s. This is substantially lower than previous studies, which reported a velocity of approximately 3 μm/s to a 70% bleach [8] and velocities approaching 3.9 and 4.6 μm/s for similar flashes [10]. We note that numerical integration is not necessary for this comparison, as the slope of the integrated curve is the same as the time-averaged velocity in the same 10 to 100 ms interval.

The effect of lateral averaging on (signal and SNR) is shown in Fig. 7. Qualitatively, the signal is visible when averaged over at least 20 μm, and noise visibly reduced above 100 μm. The SNR was higher than two when the ORG response was averaged over at least 20 μm.

4. DISCUSSION

ORG represents a new tool for ophthalmologists and vision scientists to produce meaningful and quantifiable data about human vision. The stimulus-evoked contraction and elongation of the OS has now been independently reproduced by several research groups using hardware AO and/or full-field OCT with DAC to visualize individual photoreceptors.

The conventional (non-AO) optoretinographic method demonstrated here depends on the correlated movement of neighboring tissue, and thus circumvents the need for cellular resolution and tracking. Compared to more advanced techniques, this method offers a simpler imaging system, reduced data sizes, faster signal processing, and smaller demands on personnel. One of its key advantages is potentially straightforward incorporation into existing commercial technology. The data shown in Figs. 5(a) and 5(b) required approximately 10 min per subject to acquire, including dark adaptation, and required just one operator. Our data processing software was written in a high-level language (Python/Numpy) and is thus not optimized for real-time use. Nevertheless, results are available within minutes, making the approach attractive to clinicians and large-scale studies. As shown in Fig. 6, the main result of this method—a time series of OS velocity—can be integrated to approximate the results of earlier, position-based optoretinographic methods. Congruity between the two results is an advantage to both, as they can contribute to the same growing body of literature and data. The present results reveal velocities that are lower by a factor of two to three than earlier position-based results, but the pattern of contraction and elongation demonstrated here bears significant similarity to earlier results, including the timing of the early and late stages. This suggests that the biophysical processes

underlying the responses are the same. The reason for the discrepancy in velocities is not known, but could potentially be due to optical factors such as the role played by the lateral point spread function (PSF) size and contributions of portions of the tissue that might be stationary. We are optimistic that such systematic differences between the approaches can be resolved by calibration. Compared to 2D methods (scanning or full-field, with AO or DAC), the method proposed here sacrifices areal field of view. The former methods could potentially reveal functional gradients in perilesional or transitional zones and thus provide critical insights into disease pathophysiology. Our approach would require serial imaging at different locations, or at least control over the angle of the line-scan to measure such gradients.

The clear relationship between ORG responses and distance from the fovea [Figs. 4, 5(a), and 5(b)] may be due to differences in OS anatomy, and normalizing by OS length seems to weaken this dependence. When designing the imaging protocol, we strove to avoid realignment of the optical system with changes in fixation. Given that, and the fact that this method does not require dilation of the pupil, there is a risk that the subject's iris could clip the 3.5 mm diameter stimulus beam after changing fixation. We did not actively monitor this, but it could be done with a real-time pupil camera programmed to detect iridial reflexes. Alternatively, a brighter stimulus source could be used, permitting the beam diameter at the pupil to be smaller. If the OCT and stimulus beam diameters were the same, the OCT signal itself could be used to calculate the stimulus efficiency (not withstanding chromatic differences). Moreover, because the trends were similar among subjects, regardless of which fixation target location was used for initial alignment, we do not believe that the stimulus beam was clipped.

A distinct trend was also observed when we altered the stimulus energy [Figs. 5(c) and 5(d)]. Photopigment bleaching is dependent on stimulus dosage between 8% and 66% pigment bleaching. Establishing dose dependence is a critical step in developing novel functional assays. The dose dependence observed here is consistent with similar observations of dose dependence using position-based optoretinographic methods, providing further assurance of the interoperability of these two methods.

We observed that optoretinograms were reliably produced from all tested eccentricities when the stimulus energy bleached more than 8% of the photopigment. While this sensitivity is lower than what has been reported with AO-OCT systems, the noise floor of the present method could potentially be reduced with improved bulk-motion correction. The 30 ms duration of the stimulus flash was required to reach a photopigment bleaching rate of 66%, due to limitations in the source power and our optical design. A more powerful source and redesign of the stimulus channel could permit shorter, more intense flashes, which would likely improve the method's sensitivity. The odd result in Fig. 5(c)—that v_{min} was non-zero even in the absence of a stimulus flash (0% bleaching)—may be a consequence of noise combined with the bias involved in identifying the minimum (most negative) velocity. If, for instance, the most negative pre-stimulus velocities shown in Fig. 4 were averaged, the resulting value would be negative and give the false impression that the OSs were contracting in the dark. This bias probably limits the sensitivity of this figure of merit. A better alternative may be to track the OS contraction velocity at a specific delay

post-stimulus, e.g., 10 ms, although eccentricity- and subject-dependent variations in the response dynamics would have to be studied carefully first to select the most advantageous delay.

One of the motivating assumptions of this work is that there are finite time intervals over which the retina is effectively motionless, i.e., that the axial component of motion is small with respect to the wavelength of the light source and that the lateral component is small with respect to the diffraction-limited spot size (or speckle size). While this assumption appeared largely to be true, evidence of motion artifacts was present in many of the measurements. A potentially powerful way to improve the sensitivity of this approach would be to detect and filter movement artifacts. When analyzing a series of B-scans to measure instantaneous velocity, we monitored the residual least-squares error and the correlation of B-scan amplitude. Preliminary investigation showed that both estimates of error were correlated with deviations from expected velocity measurements.

Our results reveal a biphasic ORG response, consisting of an initial contraction and later elongation of the OS. These stages of the response are thought to have different physiological origins, and may thus confer distinct clinical utilities. Zhang *et al.*, by demonstrating a lack of elongation in mutant mice with a dysfunctional G-protein transducin, suggested that transducin subunit dissociation might drive ORG elongation osmotically [20]. Pandiyan *et al.* hypothesized that the contractile response seen in the ORG is due to the early receptor potential (ERP) [10].

For optoretinograms presented here we used a simple OCT B-scan flattening procedure. In future studies, a segmentation-based approach is needed. AO studies of photoreceptor morphology [21,22] have revealed axially staggered locations of IS/OS and COST in neighboring cones. Moreover, the B-scans shown above illustrate that the ideal depth at which to measure the phase of these surfaces can change from A-scan to A-scan. Instead of computing the phase at the same depth for all A-scans, segmentation would permit measurement of phase at the most salient (and brightest) depths, and thereby improve the ORG sensitivity. It would also allow the investigation of eccentricities closer to the fovea, where the thickness of retinal layers can vary substantially within small visual angles. It could potentially help in the imaging of disease-affected retinae as well, where the layers may be sporadically deformed by edema, drusen, or degeneration.

Last, the use of a finite temporal window to calculate velocity is equivalent to convolution of the underlying signal with a rect function, which limits temporal bandwidth and causes underestimation of instantaneous velocity. Since the convolution kernel is known exactly, potential exists for computational correction of the measurements and estimation of true velocities.

We have shown that it is possible to obtain ORG responses using an OCT system without AO. The simplicity of the imaging system permits straightforward integration of this method to existing OCT systems. While more research is needed, these preliminary results indicate a promising new way to produce optoretinograms, which may pave the way for a clinical ORG system. Future work will include refinement of the optical and computational aspects

of the system, further testing of subjects with and without retinal disease, and comparison of the approach to other conventional (non-AO) imaging-based approaches [23–25].

Acknowledgment.

The authors thank Dr. Yifan Jian for providing the OCT acquisition software, Prof. John Werner for helping with theoretical calculations, and Susan Garcia for clinical assistance. Support for OCT personnel was partly funded by NIH UG1EY026879 for concurrent use in that study.

Funding.

National Institutes of Health (P30-EY-012576, R00-EY-026068, R01-EY-031098, R01-EY-033532, RO1-EY-026556, UG1EY026876).

Data availability.

Data underlying the results presented in this paper are not publicly available at this time but may be obtained from the authors upon reasonable request.

REFERENCES

1. Frishman LJ, “Origins of the electroretinogram,” in Principles and Practice of Clinical Electrophysiology of Vision, Heckenlively JR and Arden GB, eds. (MIT, 2006), pp. 139–183.
2. Drexler W and Fujimoto JG, eds., Optical Coherence Tomography, 2nd ed. (Springer, 2015).
3. Choma MA, Ellerbee AK, Yang C, Creazzo TL, and Izatt JA, “Spectral-domain phase microscopy,” Opt. Lett 30, 1162–1164 (2005). [PubMed: 15945141]
4. Makita S, Hong Y, Yamanari M, Yatagai T, and Yasuno Y, “Optical coherence angiography,” Opt. Express 14, 7821–7840 (2006). [PubMed: 19529151]
5. Jonnal RS, Kocaoglu OP, Wang Q, Lee S, and Miller DT, “Phase-sensitive imaging of the outer retina using optical coherence tomography and adaptive optics,” Biomed. Opt. Express 3, 104–124 (2012). [PubMed: 22254172]
6. Jonnal RS, Rha J, Zhang Y, Cense B, Gao W, and Miller DT, “In vivo functional imaging of human cone photoreceptors,” Opt. Express 15, 16141–16160 (2007).
7. Hillmann D, Spahr H, Pfäffle C, Sudkamp H, Franke G, and Hüttmann G, “In vivo optical imaging of physiological responses to photo-stimulation in human photoreceptors,” Proc. Natl. Acad. Sci. USA 113, 13138–13143 (2016). [PubMed: 27729536]
8. Azimipour M, Migacz JV, Zawadzki RJ, Werner JS, and Jonnal RS, “Functional retinal imaging using adaptive optics swept-source OCT at 1.6 MHz,” Optica 6, 300–303 (2019). [PubMed: 33511257]
9. Zhang F, Kurokawa K, Lassoued A, Crowell JA, and Miller DT, “Cone photoreceptor classification in the living human eye from photostimulation-induced phase dynamics,” Proc. Natl. Acad. Sci. USA 116, 7951–7956 (2019). [PubMed: 30944223]
10. Pandiyan VP, Maloney-Bertelli A, Kuchenbecker JA, Boyle KC, Ling T, Chen ZC, Park BH, Roorda A, Palanker D, and Sabesan R, “The optoretinogram reveals the primary steps of phototransduction in the living human eye,” Sci. Adv 6, eabc1124 (2020). [PubMed: 32917686]
11. Azimipour M, Valente D, Vienola KV, Werner JS, Zawadzki RJ, Jonnal RS, and Jonnal RS, “Optoretinogram: optical measurement of human cone and rod photoreceptor responses to light,” Opt. Lett 45, 4658–4661 (2020). [PubMed: 32870829]
12. Mulligan JB, MacLeod DIA, and Statler IC, “In search of an optoretinogram,” in Vision Science and Its Applications, Technical digest series (1994), Vol. 2.
13. Jonnal RS, “Toward a clinical optoretinogram: a review of noninvasive, optical tests of retinal neural function,” Ann. Transl. Med 9, 1270 (2021). [PubMed: 34532407]

14. Lassoued A, Zhang F, Kurokawa K, Liu Y, Bernucci MT, Crowell JA, and Miller DT, “Cone photoreceptor dysfunction in retinitis pigmentosa revealed by optoretinography,” Proc. Natl. Acad. Sci. USA 118, e2107444118 (2021). [PubMed: 34795055]
15. Bowmaker JK and Dartnall HJ, “Visual pigments of rods and cones in a human retina,” J. Physiol 298, 501–511 (1980). [PubMed: 7359434]
16. Jian Y, Wong K, and Sarunic MV, “Graphics processing unit accelerated optical coherence tomography processing at megahertz axial scan rate and high resolution video rate volumetric rendering,” J. Biomed. Opt 18, 026002 (2013).
17. Rushton WA and Henry GH, “Bleaching and regeneration of cone pigments in man,” Vision Res. 8, 617–631 (1968). [PubMed: 5729910]
18. Packer O and Williams DR, “Light, the retinal image, and photoreceptors,” in The Science of Color, 2nd ed., Shevell SK, ed. (Elsevier Science, 2003), pp. 41–102.
19. “American National standard for safe use of lasers,” ANSI Z136.1–2014 (Laser Institute of America, 2014).
20. Zhang P, Zawadzki RJ, Goswami M, Nguyen PT, Yarov-Yarovoy V, Burns ME, and Pugh EN, “In vivo optophysiology reveals that G-protein activation triggers osmotic swelling and increased light scattering of rod photoreceptors,” Proc. Natl. Acad. Sci. USA 114, E2937–E2946 (2017). [PubMed: 28320964]
21. Jonnal RS, Kocaoglu OP, Zawadzki RJ, Lee S-H, Werner JS, and Miller DT, “The cellular origins of the outer retinal bands in optical coherence tomography images,” Invest. Ophthalmol. Visual Sci 55, 7904–7918 (2014). [PubMed: 25324288]
22. Jonnal RS, Gorczynska I, Migacz JV, Azimipour M, Zawadzki RJ, and Werner JS, “The properties of outer retinal band three investigated with adaptive-optics optical coherence tomography,” Invest. Ophthalmol. Visual Sci 58, 4559–4568 (2017). [PubMed: 28877320]
23. Lu CD, Lee B, Schottenhamml J, Maier A, Pugh EN, and Fujimoto JG, “Photoreceptor layer thickness changes during dark adaptation observed with ultrahigh-resolution optical coherence tomography,” Invest. Ophthalmol. Visual Sci 58, 4632–4643 (2017). [PubMed: 28898357]
24. Son T, Kim T-H, Ma G, Kim H, and Yao X, “Functional intrinsic optical signal imaging for objective optoretinography of human photoreceptors,” Exp. Biol. Med 246, 639–643 (2021).
25. Ma G, Son T, Kim T-H, Yao X, and Yao X, “Functional optoretinography: concurrent OCT monitoring of intrinsic signal amplitude and phase dynamics in human photoreceptors,” Biomed. Opt. Express 12, 2661–2669 (2021). [PubMed: 34123495]

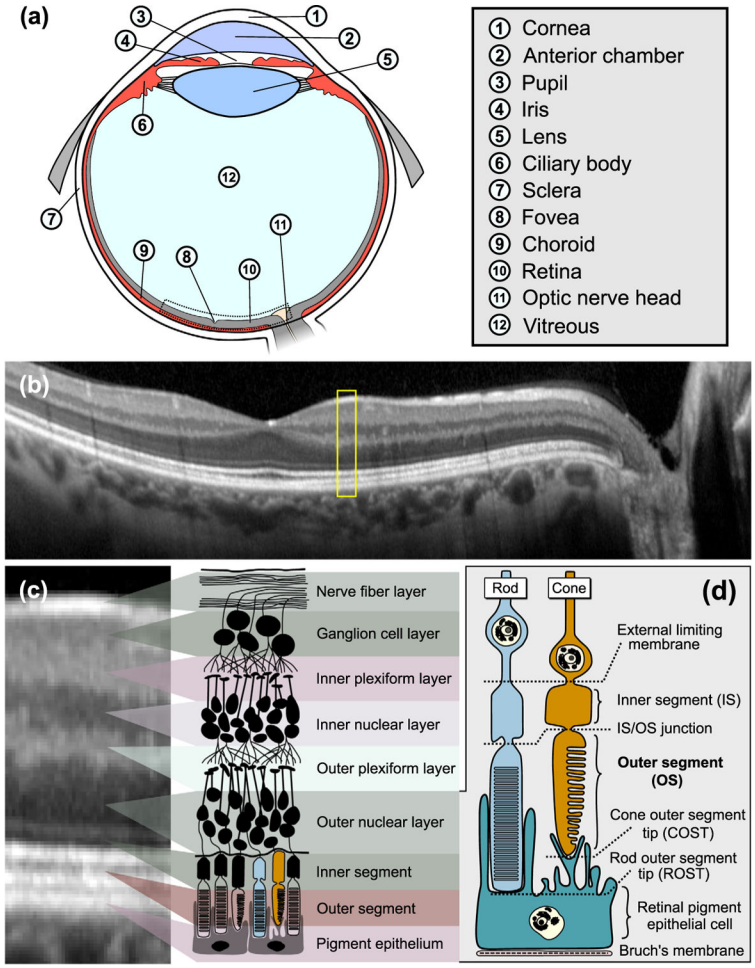

Fig. 1.

Outer segment elongation can be observed with phase-sensitive OCT. (a) Schematic of an eye indicating its key parts. (b) Wide-field B-scan of the human retina extending from temporal to nasal across fovea and optic nerve head. (c) Portion of the OCT image [indicated with a yellow box in (b)], magnified and aligned with a diagram of the layers of the retina. (d) Diagram of human photoreceptor cells illustrating subcellular anatomy. One approach to photoreceptor optoretinography monitors stimulus-evoked changes in outer segment (OS) length.

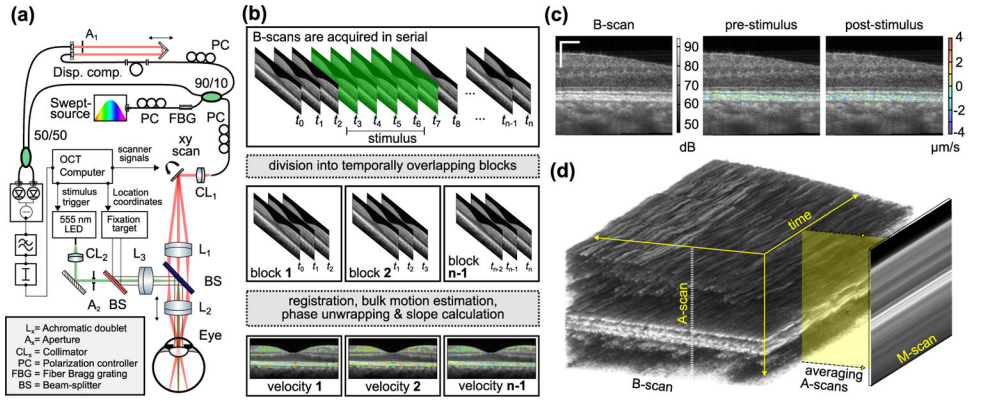

Fig. 2.

Optical layout and signal processing. (a) SS-OCT system layout (not in scale). (b) Diagram of the ORG data processing. Once the block width is selected, the phase slopes are obtained from the block data as they move (with a step size of one B-scan) through the acquired dataset. (c) These phase slopes are calculated from the block for each individual pixel in the OCT B-scan after bulk motion correction. The residual velocities in the inner retina are due to blood flow. Scale bar 125 μm. (d) M-scans are generated by averaging the amplitude and phase velocity of A-scans within each B-scan, creating an averaged depth profile over time. The depicted block size (three B-scans) and stimulus width (five B-scans) in (b) are for illustrative purposes.

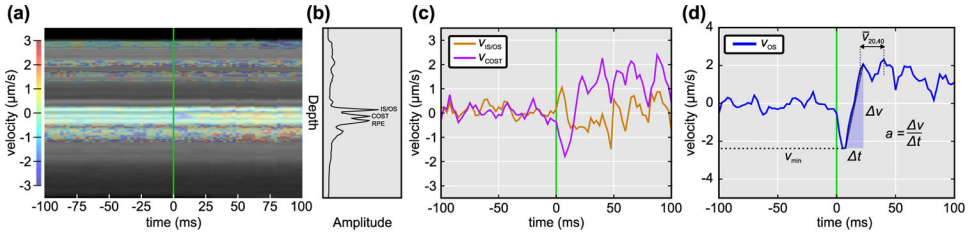

Fig. 3.

Extraction of velocity from the M-scan. (a) M-scan of a single optoretinographic measurement. The pseudocolor overlay represents the tissue velocity derived from phase slopes, and the green line indicates stimulus onset. (b) Axial depth profile produced by averaging the M-scan over time. The inner segment/outer segment junction (IS/OS) and cone outer segment tips (COST) were used for analysis. (c) Velocity plotted as a function of time for the IS/OS and COST. Both show rapid changes occurring after the stimulus flash is applied at 0 ms. (d) By subtracting the velocity responses shown in (c), we produce the outer segment elongation velocity curve. After the stimulus at 0 ms, the velocity rapidly changes; an initial contractile stage is followed by a longer period of elongation after ĩ20 ms. Also illustrated are the three approaches we explored for quantification of the OS response: minimum (i.e., most negative) velocity $v_{\min}$, average velocity from 20 to 40 ms ($\bar{v}_{20,40}$), and maximum acceleration $a_{\max}$.

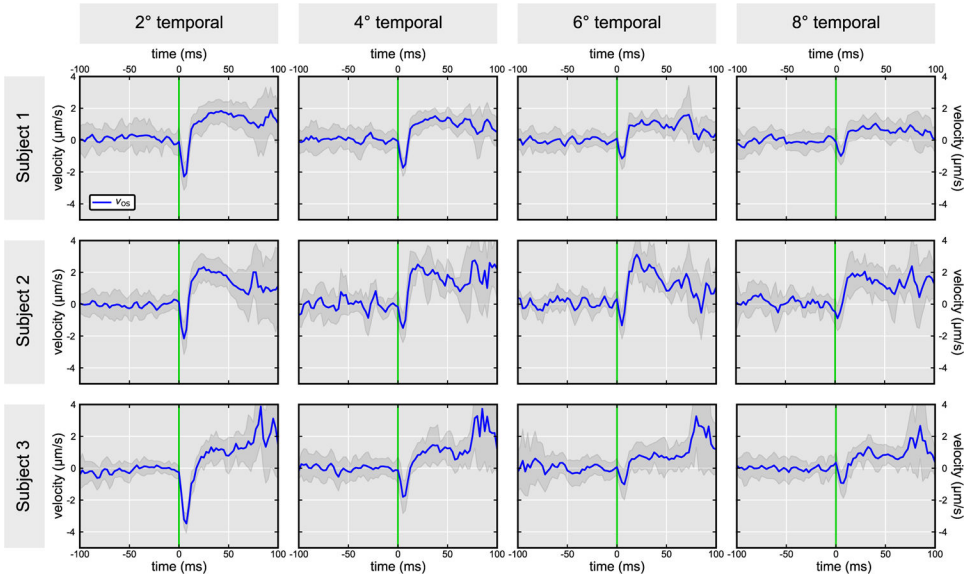

Fig. 4.

Optoretinograms from three subjects at four locations in the temporal retina. Stimulus flash onset was at 0 ms. The blue line shows the average response over five trials, with the shaded gray area indicating ± one SEM. Retinal eccentricity of the measurement (in visual angle from the foveal center) is indicated at the top. The bleaching level for all measurements was 66%. Two features were evident in all measurements: an initial negative velocity (approximately 0 to 10 ms), followed by a longer period of positive velocity (approximately 10 to >50 ms). The magnitude of both features appeared to fall with increasing retinal eccentricity. Responses appeared to become noisy after approximately 70 ms, possibly indicating the presence of reflexive eye movements.

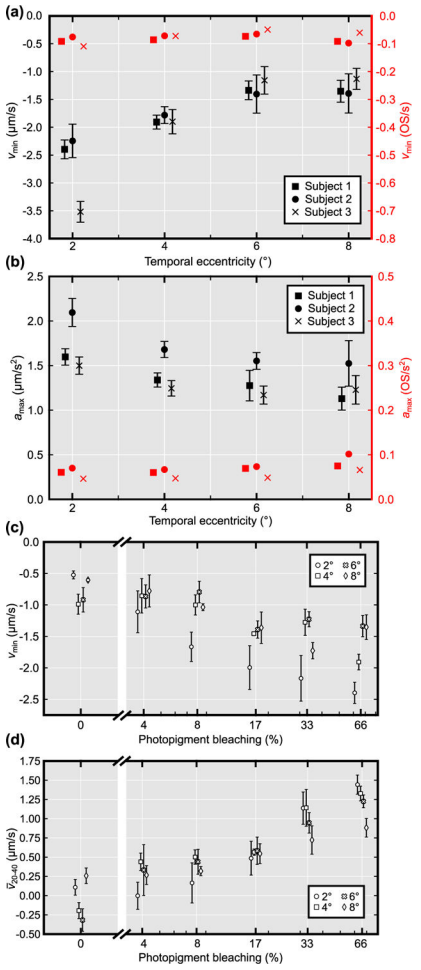

Fig. 5.

Photoreceptor ORG response as a function of eccentricity (a), (b) and pigment bleaching (c), (d). The most negative velocity (v_{min}), observed within 20 ms of stimulus onset, reduced in magnitude with increasing visual angle; the fastest OS contractions were observed closest to the foveal center, where the cone OS is longest, as shown by the black markers in (a). The maximum OS acceleration (a_{max}) was similarly highest nearest the fovea, as shown by the black markers in (b). When these two values were visualized as fractions of OS length instead of physical length, both relationships appeared to be substantially flattened, as shown by the red markers in (a) and (b). Both contraction velocity (v_{min}) and average elongation velocity from 20 to 40 ms ($\bar{v}_{20,40}$) appeared to depend on the stimulus dose, having the largest magnitudes in response to the brightest stimuli, as shown in (c) and (d), respectively. In (c), the unexpected non-zero contractile velocity in the absence of stimulus may be due to the quantitative parameter v_{min}, which will be negatively biased due to noise. Error bars indicate the standard error of the mean. They are omitted in the length-normalized plots in (a) and (b) because they were too small to be informative.

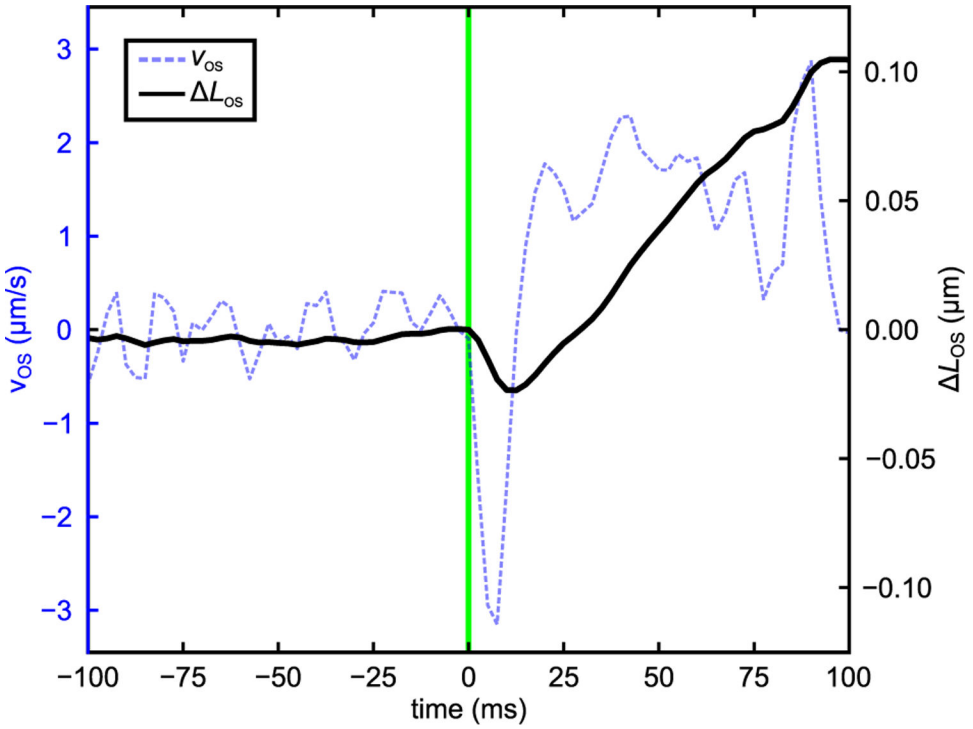

Fig. 6.

Outer segment velocity numerically integrated to reconstruct the change in OS length. The blue dashed line plotted on the left *y* axis shows an example of a response acquired at 2° temporal in subject 1, to a stimulus flash that bleached 66% of L- and M-photopigment. The black line plotted on the right *y* axis is the numerical integration from −100 to 100 ms. The slope of the resulting estimate of elongation from 20 to 100 ms is approximately 1 µm/s, lower than values reported by others using position-based methods.

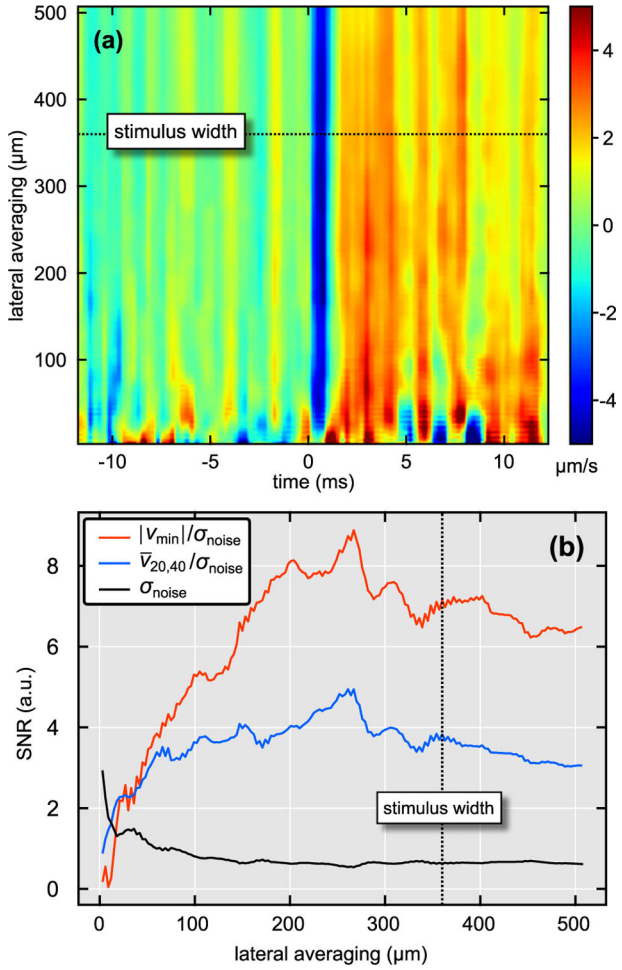

Fig. 7.

ORG response (a) and SNR (b) as functions of lateral averaging. To compute the ORG response, the phase velocities are averaged laterally over the stimulated region, leading to a potential trade-off between ORG spatial resolution and signal. (a) Rate of OS length change as a function of time and averaging length. OS contraction and elongation are clearly visible when averaging at least 20 μm, although the pre-stimulus noise is visibly higher when averaging less than 100 μm. (b) Pre-stimulus RMS of OS velocity (σ_{noise}), and the ratios of two figures of merit (v_{min} and $\bar{v}_{20,40}$) to σ_{noise}, i.e., SNR for those signals. Required SNR is probably application specific, but it is noteworthy that 20 μm averaging yields an SNR of two.

Table 1.

Different Parameters Obtained from Photopigment Bleaching Calculations[a]

Bleaching [%]	Power [μW]	Photon Count ($\times 10^{11}$)	Photon Density [photons/μm^2]
66	45	37.7181	3.7×10^7
33	16.5	13.8300	1.4×10^7
17	7.7	6.4540	6.3×10^6
8	3.45	2.8917	2.8×10^6
4	1.7	1.4249	1.4×10^6

[a]All calculations were done with a pulse width of 30 ms. For simplicity, ocular transmission was assumed to be one.